

## Many-body molecule formation at a domain wall in a one-dimensional strongly interacting ultracold Fermi gas

Andrzej Syrwid <sup>1</sup>, Maciej Łebek <sup>2,3</sup>, Piotr T. Grochowski <sup>2,\*</sup> and Kazimierz Rzażewski <sup>2</sup>

<sup>1</sup>*Department of Physics, KTH Royal Institute of Technology, SE-106 91 Stockholm, Sweden*

<sup>2</sup>*Center for Theoretical Physics, Polish Academy of Sciences, Aleja Lotników 32/46, 02-668 Warsaw, Poland*

<sup>3</sup>*Institute of Theoretical Physics, University of Warsaw, Pasteura 5, 02-093 Warsaw, Poland*

 (Received 12 May 2021; revised 12 October 2021; accepted 6 January 2022; published 18 January 2022)

We analyze how the presence of the bound state on top of strong intercomponent contact repulsion affects the dynamics of a two-component ultracold Fermi gas confined in a one-dimensional harmonic trap. By performing full many-body numerical calculations, we retrieve dynamics of an initially phase-separated state that has been utilized to excite the spin-dipole mode in experimental settings. We observe an appearance of pairing correlations at the domain wall, heralding the onset of a molecular fraction at the interlayer between the components.

DOI: [10.1103/PhysRevA.105.013314](https://doi.org/10.1103/PhysRevA.105.013314)

### I. INTRODUCTION

For decades, investigations of multicomponent mixtures have provided deep insight into details of intercomponent interplay. Specifically, an effective repulsion between constituents may result in their spatial separation [1,2] and induce an itinerant ferromagnetism in metals [3,4], where electrons spontaneously form extended, spin-polarized domains. This phenomenon was explained by the Stoner model, where a short-ranged screened Coulomb repulsion overcomes the Fermi pressure that favors a paramagnetic state [5]. While the simplified Stoner approach qualitatively describes many-electron systems, it does not capture effects related to beyond short-range interactions that may promote different, competing mechanisms suppressing ferromagnetism [6,7].

Here we investigate a two-component atomic Fermi gas with tunable short-range repulsive interactions, for which the stability of a ferromagnetic state has been debated both in theory [8–26] and in experiment [27–34]. It stems from the fact that repulsive interactions due to the Feshbach resonance support a weakly bound molecular state [35]. Then, ferromagnetic correlations appear only in an excited state of the many-body system, in contrast to the superfluid ground state of paired atoms.

Since the late 2000s, experiments have tried to settle whether pairing processes prevent the ferromagnetic domains from appearing. In the initial attempts, some signatures, such as increase of a kinetic energy, suggested the onset of ferromagnetism; however, these efforts proved inconclusive [29,31]. Only after the system was initialized in an artificial domain structure did the phase separation undoubtedly persist for some finite time in a strong interaction regime [30,33]. Recently, time-resolved investigation provided deeper insight into many-body dynamics of a quenched system [34,36].

On the theory side, approaches neglecting pairing processes showed that a ferromagnetic transition should occur in a three-dimensional (3D) geometry [10,12,14,15,37–42]. However, pairing was included either only at the mean-field level or by the introduction of phenomenological terms. In the context of Stoner ferromagnetism, many-body eigenstates of small one-dimensional (1D) contact interacting systems were analyzed [43–46]. Nevertheless, in such a case the pairing is supported only by purely attractive interactions in the absence of the repulsive core characterizing realistic atomic potentials. To capture short-range details of the interatomic potential in 1D, we utilize the so-called three- $\delta$  potential [47–54]:

$$W_{\uparrow\downarrow}(x) = c_0\delta(x) + c_\ell\delta(x - \ell) + c_\ell\delta(x + \ell), \quad (1)$$

where  $x$  denotes the relative position between opposite spin fermions. The parameters  $c_0 > 0$  and  $c_\ell < 0$  describe contact repulsion and finite-range attraction at a distance  $\ell$ , respectively. It can be understood as a first correction to the contact repulsion due to finite-range interactions and was shown to reproduce van der Waals forces under quasi-1D confinement [54] in the limit of weak interactions. Note that the potential (1) should be realizable in optical lattices where the peripheral  $\delta$ s would play a role of nearest neighbor interactions. Additionally, the intracomponent interactions are assumed to be negligible, as the considered ultracold system is brought close to the Feshbach resonance of opposite spins. Therefore, in the considered two-component (spin- $\uparrow$  and spin- $\downarrow$ ) model, intracomponent interactions are excluded and fermions belonging to the  $\uparrow$  ( $\downarrow$ ) component can interact only with fermions possessing opposite spin, i.e.,  $\downarrow$  ( $\uparrow$ ). The paradigmatic scenario analyzed here involves a strongly repulsive core with a weakly attractive well ( $0 < -c_\ell \ll c_0$ ). Our aim is to explore dynamics of two initially separated Fermi clouds—a setup inspired by former experiments [33,55,56]; see Fig. 3(b). We argue that the potential  $W(x)$  can give insight to many-body processes involved in the competition between pairing and ferromagnetic instabilities.

\*piotr@cft.edu.pl

The paper is organized as follows. We start with presenting the details of the considered model. We discuss the most important features of the employed interaction potential (1) and its range of applicability. This is followed by the ground-state analysis with a special focus on the two-body problem relevant for pairing processes. The many-body problem is studied numerically. Next, we move to the dynamics of the initially phase-separated state. We introduce relevant correlation functions and other observables used to study pairing between opposite-spin fermions. In our results, we observe qualitative differences between the dynamics of two fermions in comparison to the systems involving more particles. This can be attributed to the fact that conservation laws prohibit molecule formation in the two-body systems. Interestingly, for strong finite-range attractive interactions we find signatures of the super-Tonks-Girardeau physics suppressing pairing processes between fermions belonging to different components.

## II. MODEL

Mapping continuous, extended interactions onto discrete set of  $\delta$  potentials was first analyzed in the 1980s [47–49]. It was soon realized that the three- $\delta$  potential is a minimal extension of a realistic short-range potential between atoms [50,51] and was later utilized to study extended versions of the Gross-Pitaevskii and Lieb-Liniger models [52,53]. Recently, it was shown that the three- $\delta$  potential provides valuable insight into the qualitative behavior of the many-body system that goes beyond standard contact interactions and quantitatively reproduces scattering properties of quasi-1D dilute bosons with not very strong interactions [54]. There, the scattering theory implies  $c_0 + 2c_\ell = g_{1D}$ , where  $g_{1D}$  is a 1D coupling constant (see Appendix D). In Ref. [54], the relation between the three- $\delta$  potential parameters and the scattering ones ( $s$ -wave scattering length, effective range) was established. However, such a map was ambiguous, as some additional parameter was needed, e.g., energy of the bound state or the  $p$ -wave scattering volume. We leave this ambiguity on purpose to study effect of interatomic potential short-range details on systems usually described only in terms of  $s$ -wave scattering properties—the strength of the beyond-contact attraction is treated as a free parameter.

It needs to be noted that in the regime of strong interactions,  $mg_{1D}\ell/\hbar^2 \gg 1$ , the comparison to quasi-1D dilute gases showed spurious transmission peaks, suggesting that the use of the three- $\delta$  potential might be limited in ultracold settings. Yet, we still argue that it may give insights into qualitative behavior of such systems, while potentially providing quantitative description in more complex, e.g., molecular or optical lattice, systems. Specifically, in the latter case, such a model should be attainable, with on-site and nearest neighbor interactions being optically tuned.

For  $\ell$  much smaller than other system length scales, it was shown that a simple contact interaction description can be retrieved with the effective coupling constant  $c_{\text{eff}} = g_{1D} + \text{corrections}$  depending on  $\ell$ ,  $c_0$ ,  $c_\ell$ ; see Ref. [53]. In our work, the length scale associated with  $\ell$  is finite, which affects the system beyond the contact approximation. Intuitively, the length scale  $\ell$  should reflect a range of the real interatomic potential, but in our analysis it is much larger. Thus, the scal-

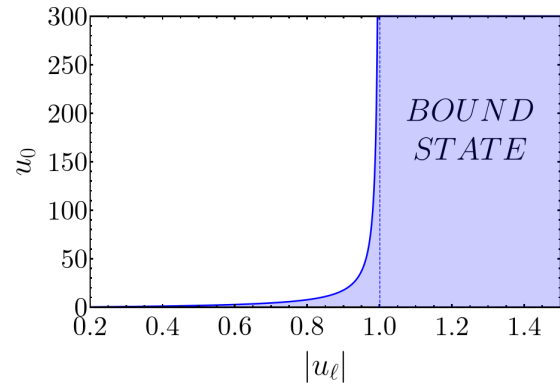


FIG. 1. Diagram of a bound-state existence for the  $M = 1$  system. Shaded area represents the region of dimensionless parameters  $u_0 = mc_0\ell/\hbar^2$ ,  $u_\ell = mc_\ell\ell/\hbar^2$  where a bound state exists. Dashed line marks the critical value  $u_\ell^{\text{crit}} = -1$  below which the three- $\delta$  potential has a bound state no matter how strong the short-range repulsion  $u_0$  is.

ing with decreasing  $\ell$  needs to be addressed. The many-body simulations we performed (see Sec. IV B) are not attainable for significantly larger number of sites that would allow for studies of the system behavior when  $\ell$  is smaller. Nevertheless, we have found no evidence of qualitative differences when  $\ell$  was increased twice and other parameters were adequately rescaled. This may suggest that our findings hold also if smaller—and more realistic in unconstrained atomic systems—values of  $\ell$  were to be used.

## III. GROUND STATE

### A. Two-body case

Our considerations are restricted to a balanced system consisting of  $M$  identical fermions with mass  $m$  in each of spin- $\uparrow$  and spin- $\downarrow$  components. The ground state may be investigated analytically in the  $M = 1$  case both for a free space and a harmonic potential confinement characterized by  $\omega$  frequency,  $U(x) = \frac{1}{2}m\omega^2x^2$  (for details, see Appendixes A and B). The Hamiltonian reads

$$H = -\frac{\hbar^2}{2m}(\partial_x^2 + \partial_y^2) + V(x) + V(y) + W_{\uparrow\downarrow}(x - y), \quad (2)$$

where either  $V(x) = U(x)$  or  $V(x) = 0$ . The corresponding two-body Schrödinger equation can be exactly solved by introducing center of mass (c.m.)  $R = (x + y)/\sqrt{2}$  and relative  $r = (x - y)/\sqrt{2}$  coordinates. In particular, we may determine values of parameters  $c_0$ ,  $c_\ell$  and  $\ell$  for which the ground-state energy becomes negative. The diagram of the bound-state existence determined for a free space case is presented in Fig. 1.

While the pointlike repulsion characterized by  $c_0$  is assumed to be extremely strong, we modify the weak attraction strength  $c_\ell$ . Consequently, a ground-state wave function  $\Psi(x_\uparrow, x_\downarrow)$  has a distinct cusp along  $x_\uparrow = x_\downarrow$ . However, an increase of  $|c_\ell|$  entails an enhancement of  $|\Psi|^2$  around  $|x_\uparrow - x_\downarrow| \approx \ell$ , which is a premise of a bound-state formation. Indeed, by energy considerations we found that for each  $c_0$  there exists some critical value of  $c_\ell$  below which  $\Psi$  represents

a bound state. As we show later, many-body dynamics of initially separated components with  $M > 1$  reveals a similar probability density accumulation for finding two fermions with opposite spins at a distance  $\ell$ , heralding the onset of the bound state.

### B. Lowest order constrained variational approximation

For large  $M$ , the many-body ground state can be studied within the lowest order constrained variational (LOCV) approximation [37,57–62]. Within this approach, the balanced gas,  $M = N/2$ , in a free space is described by the following Hamiltonian,

$$H = -\frac{\hbar^2}{2m} \sum_{i,\sigma} \partial_{x_i^\sigma}^2 + \sum_{i,j} W(x_i^\uparrow - x_j^\downarrow), \quad (3)$$

where  $x_i^\sigma$  denotes a spatial coordinate of spin- $\sigma$  atom labeled by  $i \in \{1, \dots, M\}$  and  $W(r)$  is a short-range two-body interaction potential between particles belonging to different spin components, with no spin flipping allowed. Here, the total wave function is approximated by means of the Jastrow-Slater ansatz [63],

$$\Psi(\{x_i^\uparrow\}, \{x_j^\downarrow\}) = J(\{x_i^\uparrow\}, \{x_j^\downarrow\}) \prod_{\sigma} \mathcal{D}_{\sigma}(\{x_i^{\sigma}\}), \quad (4)$$

where  $\mathcal{D}_{\uparrow}$  and  $\mathcal{D}_{\downarrow}$  are Slater determinants,

$$\mathcal{D}_{\sigma}(\{x_i^{\sigma}\}) = \frac{1}{\sqrt{M!}} \begin{vmatrix} \varphi_1^{\sigma}(x_1^{\sigma}) & \dots & \varphi_1^{\sigma}(x_M^{\sigma}) \\ \vdots & & \vdots \\ \varphi_M^{\sigma}(x_1^{\sigma}) & \dots & \varphi_M^{\sigma}(x_M^{\sigma}) \end{vmatrix}, \quad (5)$$

of plane waves  $\varphi_i^{\sigma}$ , and  $J$  is the so-called Jastrow factor,

$$J(\{x_i^\uparrow\}, \{x_j^\downarrow\}) = \prod_{i,j} f(|x_i^\uparrow - x_j^\downarrow|), \quad (6)$$

with  $f$  being a Jastrow function that accounts for a two-body relative wave function of opposite spin atoms. Such an ansatz is not valid for general Fermi systems, e.g., neutron matter; however, it proved to be a good approximation for cold atomic systems in which short-range interactions are dominant [23,37].

We assume that the Jastrow factor slightly modifies the whole wave function at short relative distances only and that the parameter  $F_{ij} = f^*(|x_i^\uparrow - x_j^\downarrow|)f(|x_i^\uparrow - x_j^\downarrow|) - 1$  is small. Thus, we can expand  $|J|^2 = 1 + \sum_{i,j} F_{ij} + O(F^2)$ .

Let us proceed to evaluate the normalization of the wave function. By the orthonormality of plane waves, we find that up to the first order in  $F_{ij}$ ,  $n \int dr |f(r)|^2 = N$ , where  $r = x - y$  is the relative coordinate and  $n_{\sigma} = n/2$  denotes the  $\sigma$ -particle density.

Now, we need to introduce physical assumptions on the behavior of the Jastrow function. We demand that for long separations between the atoms,  $J$  asymptotically tends to 1 not to affect the long-range behavior of the wave function. Even more than that, we introduce the healing length  $\xi$  that is of order of average interparticle separation  $1/n$  beyond which the Jastrow function does not modify  $\Psi$ . It expresses the intuition that on average only the nearest neighbors of opposite

spins are correlated and the correlations with atoms at longer distances are negligible. This constraint and the requirement for smoothness at the healing distance, i.e.,  $f(|r| \geq \xi) = 1$  and  $f'(\xi) = f'(-\xi) = 0$ , are two out of three constraining conditions. The last one comes from the normalization of the Jastrow factor. We assume that  $f$  deviates from 1 only inside the sphere with radius  $\xi$ ,  $K(\xi)$ , and on average there is only a single  $\uparrow\downarrow$  pair inside  $K(\xi)$ . Therefore, starting with  $n \int dr |f(r)|^2 = N$ , assuming  $L$  to be the system size, one rewrites

$$\frac{n}{2} \left[ \int_{K(\xi)} dr |f(r)|^2 + \int_{V-K(\xi)} dr 1 \right] = \frac{N}{2}, \quad (7)$$

which by noting that  $\int_{V-K(\xi)} dr = (1 - 2/N)L$  results in the last constraint:  $\frac{n}{2} \int_{K(\xi)} dr |f(r)|^2 = 1$ .

These three constraints are needed in variational calculations in order to reproduce the experimental data [37,57]. Unconstrained calculations were utilized to study nuclear matter; however, each time the Jastrow function tended to be unphysically long ranged. On the other hand, constrained studies provided an extremely good fit to the experimental data [62,64]. Note that introduction of these constraints will also imply some kind of the effective two-body interaction. If the Jastrow function were to satisfy the usual two-body Schrödinger equation for the relative wave function, it would not tend to 1 for long distances. Therefore, some kind of alternation of interaction is needed in order to satisfy the constraints, which will be addressed later.

We will now proceed to evaluate the energy within the Slater-Jastrow ansatz. The noninteracting contribution comes from the kinetic energy of the orbitals and in large atom number limit is equal to  $E_0/L = nE_F/3$ , where the Fermi energy  $E_F = \hbar^2 \pi^2 n^2 L/8m$ . The interaction part comes as a two-body cluster expansion of the total energy that takes into account both the kinetic energy from the Jastrow function and the influence of a bare two-body potential. Namely, since  $E_{\text{int}} = \langle \hat{H} \rangle - E_0$ , one finds

$$\frac{E_{\text{int}}}{L} \approx n_{\uparrow} n_{\downarrow} \int dr f^*(r) \left( -\frac{\hbar^2}{2\mu} \partial_r^2 + W(r) \right) f(r). \quad (8)$$

Now, Eq. (8) needs to be extremized with respect to variations of  $f$ . However, in order for  $f$  to satisfy the constraints, two-body interaction needs to be altered. The easiest way to do so is by adding additional constant external potential  $\lambda$  in such a way that  $W \rightarrow W - \lambda$  [64]. It is not the only way of renormalization, but it was shown to provide reliable results and to be equivalent to the so-called Moszkowski-Scott separation [65] and Brueckner theory [66]. This procedure can be understood as an effect of average pressure of further neighbors and sometimes it is interpreted as a contribution of two-body correlations to average field felt by a given atom.

Therefore, to find a minimum, one needs to solve  $\delta E_{\text{int}} = 0$  with  $E_{\text{int}}$  (8) where  $W \rightarrow W - \lambda$ , which yields the following two-body Schrödinger-like equation,

$$-\left[ \frac{\hbar^2}{2\mu} \partial_r^2 + W(r) \right] f(r) = \lambda f(r), \quad (9)$$

that needs to be solved with the above-mentioned constraints.

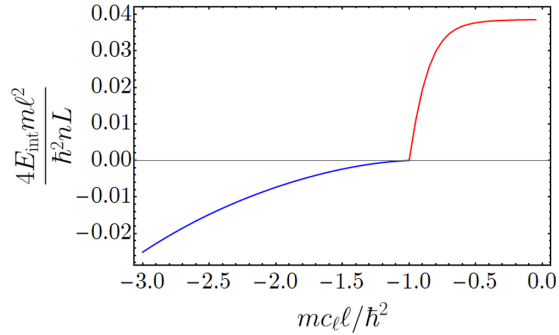


FIG. 2. Interaction energy of the ground state within the LOCV approximation for  $n\ell = 0.25$ . The sharp transition from positive to negative energy is clearly visible at  $mc_\ell\ell/\hbar^2 \approx -1$  and indicates an appearance of the bound state in the system.

Finally, we find  $E_{\text{int}}/L = n\lambda/2$ , which indicates that on average we have  $n/2$  pairs, each one contributing energy  $\lambda$ .

The LOCV approximation proved to provide reliable experimental predictions in many settings, from dense nuclear matter to ultracold quantum mixtures. However, it was mostly utilized in three-dimensional geometries, in which the level of its accuracy matches state-of-the-art quantum Monte Carlo calculations [37,62]. Analysis of low-dimensional systems was scarce, but the preliminary results in two-dimensional Fermi gas suggest that LOCV fares worse in such geometries. The probable reason is a larger role of quantum fluctuations in lower dimensions and the resulting need to go beyond the lowest order in the cluster expansion to match the more sensitive approaches. Nevertheless, the qualitative match can be expected as LOCV should reproduce leading-order behavior of systems considered.

We have performed calculations for the system with three- $\delta$  interactions  $W_{\uparrow\downarrow}$  within the LOCV approximation (for details, see Appendix C). Taking the limit  $c_0 \rightarrow \infty$ , we found that the interaction energy in the ground state within the LOCV approximation becomes negative for  $c_\ell \leq c_{\text{crit}} = -\frac{\hbar^2}{m\ell}$  (see Fig. 2). Note that the critical value  $c_{\text{crit}}$  does not depend on  $M$ , corresponding to  $c_{\text{eff}} = 0$  from Ref. [53].

In agreement with LOCV, the analysis of the two-body Schrödinger equation specifies  $c_{\text{crit}}$  as a boundary value of interaction below which in the limit  $c_0 \rightarrow \infty$  there exists a bound state [see Fig. 1(a)]. Therefore, when crossing  $c_{\text{crit}}$ , we expect to observe a change of dynamical behavior of the initially separated ferromagnetic state, as signatures of bound structures may appear.

#### IV. DYNAMICS

We now proceed to study dynamical properties of the initially phase-separated system, where the components are confined to their respective halves of the trap due to a high potential barrier in the center. Both components do not have any meaningful overlap and are effectively noninteracting. The barrier is then instantaneously released and the system evolves freely. As the intercomponent overlap starts to accumulate, the corresponding correlations begin to appear around the trap center.

#### A. Two-body dynamics

First, we focus on  $M = 1$  case which can be analyzed analytically, again thanks to the separation of c.m. and relative coordinates (see Appendix B for details). The eigenstates take the form

$$\Psi_{n,\mu}(x, y) = \phi_n\left(\frac{x+y}{\sqrt{2}}\right)\psi_\mu\left(\frac{x-y}{\sqrt{2}}\right), \quad (10)$$

where  $\phi_n$ ,  $n = 0, 1, 2, \dots$  is a harmonic oscillator eigenstate whereas  $\psi_\mu$  represents an eigenstate of  $H_{\text{rel}}$ . The evolution of the initially separated state is obtained via

$$\Psi(x, y; t) = \sum_{n,\mu} e^{-\frac{i}{\hbar}E_{n,\mu}t} C_{n,\mu} \Psi_{n,\mu}(x, y) \quad (11)$$

Here  $C_{n,\mu} = \langle \Psi_{n,\mu} | \Psi_0 \rangle$  and the initial state corresponding to two atoms separated with an infinitely high and very thin potential barrier reads

$$\Psi_0(x, y) = 2\phi_1(x)\phi_1(y)\theta(x)\theta(-y), \quad (12)$$

with  $\theta(x)$  denoting the Heaviside step function. We stick to the case in which  $\ell/d \approx 0.238$ , where  $d = \sqrt{\hbar/m\omega}$  is the harmonic trap length. For convenience, the following dimensionless interaction parameters,  $\gamma_\alpha = 2^{1/4} \frac{c_\alpha}{d\hbar\omega}$  with  $\alpha = 0, \ell, \text{crit}$ , are utilized. Throughout our analysis, the repulsive core constant is set to  $\gamma_0 = 100$  ( $\gamma_0 \gg |\gamma_\ell|$ ), corresponding to large  $g_{1D}$ , which guarantees a phase separation of fermionic clouds at the mean-field level.

Despite  $|\gamma_\ell| \ll \gamma_0$ , the beyond-contact attraction has dramatic consequences on the system dynamics. When it is sufficiently weak, the preservation of the initial phase separation is guaranteed over several trap periods due to the central core repulsion; cf. Fig. 3(d). Note that in 1D systems phase separation is never infinitely stable for finite interactions and the initial domain structure will eventually melt [67]; however, we are focused on much shorter timescales, during which the phase separation is supported.

Surprisingly, the initial domain structure is also preserved when the finite-range attraction is sufficiently strong; see Fig. 3(f). The relevant mechanism responsible for such a behavior was studied in detail in Ref. [68] and has a lot in common with the super-Tonks-Girardeau gas phase [69,70]. The origins of metastability in the regime of large, negative  $\gamma_\ell$  may be understood by looking at the spectrum of the relative part of the Hamiltonian.

We consider the limit  $\gamma_0 \rightarrow \infty$ , fix  $\ell/d = 0.2$ , and analyze the spectrum as a function of  $c_\ell$ . Due to infinite contact repulsion, the spectrum is double degenerate and states may be grouped into pairs consisting of one symmetric and antisymmetric characterized by equal energies. Similarly to purely contact interactions [68,71], there is a relation between spectra in the limits  $c_\ell \rightarrow \pm\infty$ . Namely, the spectrum of relative Hamiltonian in the strongly attractive case consists of eigenstates of the  $c_\ell \rightarrow \infty$  regime supplemented by two deep bound states with negative, diverging energy (cf. Fig. 4). In general, the dynamics of the system is given by (11). Let us focus on the case  $c_\ell/\hbar\omega d \rightarrow -\infty$ . As the initial state,  $\Psi_0$ , corresponds to two initially separated atoms, the wave function is zero when  $x = y$  and is still very small for  $|x - y| = \ell$ . On the other hand, the bound states,  $\Psi_b$ , are tightly

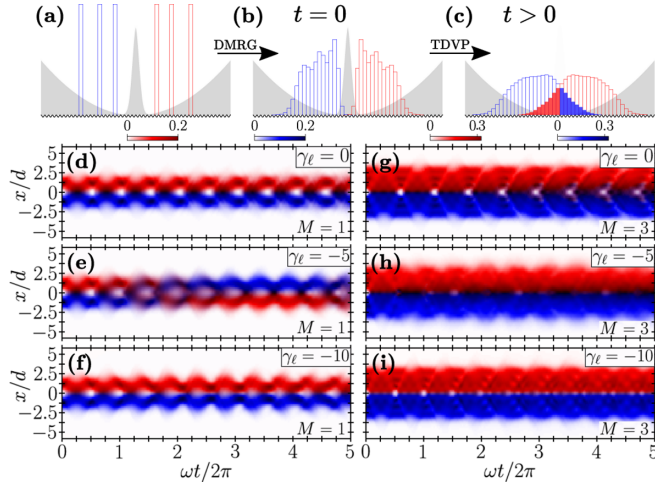


FIG. 3. Illustration of how the phase separated state with  $M = 3$  is prepared [(a), (b)] and then subsequently evolved after the removal of the central barrier (c). Time evolution of particle densities (normalized to a number of particles  $M$ ) of two Fermi components interacting via the three-delta potential obtained for  $M = 1$  [(d)–(f)] and  $M = 3$  [(g)–(i)]. In the considered timescales, for sufficiently weak and sufficiently strong beyond-contact attraction  $\gamma_\ell$ , the domain structure is stabilized for both  $M = 1$  and  $M = 3$ . In contrast to the  $M = 1$  case, at the moderate attraction ( $\gamma_\ell \approx \gamma_{\text{crit}} = -5$ ),  $M = 3$  system remains separated.

localized at  $|x - y| = \ell$  and almost zero elsewhere. Consequently,  $\langle \Psi_0 | \Psi_b \rangle \rightarrow 0$  and both symmetric and antisymmetric bound states effectively do not contribute to the dynamics (11). The remaining states that do have a meaningful overlaps, are at the same time eigenstates of the system with  $c_\ell/\hbar\omega d \rightarrow \infty$ . As a result, the dynamics of the system with strong finite-range attraction closely follows the dynamics of the system with strongly repulsive potential  $c_\ell/\hbar\omega d \rightarrow \infty$ . Further analysis of this mechanism is provided in Ref. [68]. On the other hand, intermediate regime,  $\gamma_\ell \approx \gamma_{\text{crit}}$ , does not support the short-time stabilization of the spatial separation, as atoms mix with each other; cf. Fig. 3(e). It can be explained

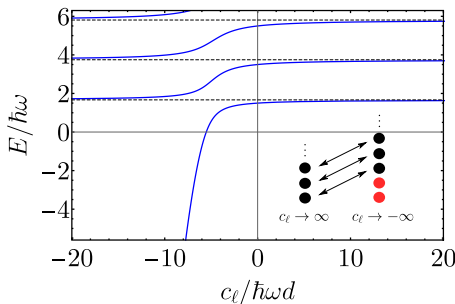


FIG. 4. The spectrum of the relative part of the Hamiltonian in the limit  $c_0/\hbar\omega d \rightarrow \infty$  for  $\ell/d = 0.2$  as a function of  $c_\ell$ . Due to the degeneracy, each curve corresponds to two states: Symmetric and antisymmetric. There are two bound states (symmetric and antisymmetric) for sufficiently negative  $c_\ell/\hbar\omega d$ . The inset presents a pictorial representation of the relationship between spectra for  $c_\ell/\hbar\omega d \rightarrow \infty$  and  $c_\ell/\hbar\omega d \rightarrow -\infty$ , where red dots represent bound states.

through the involvement of the bound state in the dynamics. Indeed, by examining Fig. 4, one can see that the fastest spin dynamics happens in the region close to the avoided crossing between the bound states and the excited states at  $\gamma_\ell \approx \gamma_{\text{crit}}$ .

Let us now proceed to a similar analysis in the few-body system.

## B. Many-body dynamics

In order to tackle the many-body problem, we first discretize the following Hamiltonian,

$$\hat{H} = \sum_{\sigma=\uparrow,\downarrow} \int dx \hat{\psi}_\sigma^\dagger(x) \left[ -\frac{\hbar^2}{2m} \partial_x^2 + \frac{1}{2} m \omega^2 x^2 \right] \hat{\psi}_\sigma(x) + \int dxdy \hat{\psi}_\uparrow^\dagger(x) \hat{\psi}_\downarrow^\dagger(y) W_{\uparrow\downarrow}(x-y) \hat{\psi}_\uparrow(x) \hat{\psi}_\downarrow(y), \quad (13)$$

where  $\hat{\psi}_\sigma(x)$  denotes the canonical Fermi field annihilation operator satisfying standard fermionic anticommutation relations. To do so, we switch from the continuous space to the lattice consisting of  $N_s$  sites with spacing  $\Delta$  and introduce new fermionic operators acting directly on lattice sites, i.e.,  $\hat{\psi}_\sigma(x_i) \rightarrow \sqrt{\Delta} \hat{a}_{\sigma,i}$ , where  $x_i$  represents a position of  $i$ th lattice site. In result, we arrive at the Fermi-Hubbard (FH) model with beyond on-site interactions

$$\hat{H}_{\text{FH}} = \mathcal{T} \sum_{\sigma,i} (\hat{a}_{\sigma,i}^\dagger \hat{a}_{\sigma,i+1} - \hat{n}_{\sigma,i} + \text{H.c.}) + \mathcal{U} \sum_{\sigma,i} x_i^2 \hat{n}_{\sigma,i} + \sum_i \left( \frac{c_0}{\Delta} \hat{n}_{\uparrow,i} \hat{n}_{\downarrow,i} + \frac{c_\ell}{\Delta} \hat{n}_{\uparrow,i} \hat{n}_{\downarrow,i+s} + \frac{c_\ell}{\Delta} \hat{n}_{\uparrow,i+s} \hat{n}_{\downarrow,i} \right), \quad (14)$$

where  $\mathcal{T} = \hbar^2/2m\Delta^2$ ,  $\mathcal{U} = m\omega^2/2$ ,  $\hat{n}_{\sigma,i} = \hat{a}_{\sigma,i}^\dagger \hat{a}_{\sigma,i}$  is the spin- $\sigma$  particle number operator at site  $i$ , and  $s$  represents the distance  $\ell$  in lattice sites, i.e.,  $\ell = s\Delta$ . Here, for the purpose of our analysis we set  $s = 1$ . Therefore, the contact interaction becomes the on-site one, while peripheral  $\delta s$  correspond to the nearest neighbor attraction. More specifically, we use the units where  $\hbar = m = 1$  and restrict ourselves to the lattice system of size  $L = 10$  and  $N_s = 50$  sites. The lattice spacing  $\Delta$  equals the distance between  $\delta s$ , i.e.,  $\Delta = L/N_s = \ell = 0.2$ . To investigate the many-body dynamics, we employ matrix product states (MPS) [72,73] ansatz with open boundary conditions, where we assumed that the system edges and lattice site positions are located at  $x_{\text{OBC}} = \pm L/2$  and  $x_{j=1,\dots,N_s} = -L/2 + \Delta(j - 1/2)$ , respectively. The harmonic confinement is realized by employing the trap of frequency  $\omega = \sqrt{2}$  centered at  $x = 0$ , which guarantees that particles in the systems under considerations ( $M \leq 3$ ) never feel the hard-wall boundaries. The initially separated state is prepared with the help of a standard density matrix renormalization group (DMRG) method [72–76] in the presence of a Gaussian barrier  $V_b(x) = A e^{-x^2/2\sigma^2}$ , starting with a state where fermions of opposite spins occupy sites in different halves of the trap far from  $x = 0$ ; cf. Fig. 3(a). For this purpose, we used  $A = 10(M + 1)$  and  $\sigma = \ell$ . It yields a matrix product state (MPS) in which the clouds of atoms belonging to different components are well separated and they are mirror images of each other with respect to the trap center; cf. Fig. 3(b). After removing the

barrier at time  $t = 0$ , the system dynamics is investigated with the help of an algorithm combining one-site time-dependent variational principle (TDVP) procedure [77] and a global basis expansion [78]; cf. Fig. 3(c).

Generally, time evolution within the MPS approach is error prone and computationally demanding. It is due to the fact that together with a ballistic increase of an entanglement entropy in the course of dynamics, it is required to deal with increasing bond dimension. This issue was partially overcome by a recent development of the time-dependent variational principle (TDVP) algorithm [79–81], which allows for a time propagation with a fixed bond dimension (one-site TDVP). It is much less error prone in comparison with other earlier techniques like the time-evolving block decimation (TEBD) routine [82]. Nevertheless, to reproduce a system dynamics properly, the bond dimension has to be first enlarged enough, which can be done, for example, as in the “hybrid” TDVP strategy, where the desired bond dimension is obtained through the initial application of the two-site TDVP scheme [82–84]. Here, we employ a recent approach in which the basis for MPS  $|\Psi\rangle$  is enlarged by means of a subspace expansion by global Krylov vectors  $\{|\Psi\rangle, \hat{H}|\Psi\rangle, \dots, \hat{H}^{k-1}|\Psi\rangle\}$ , where  $\hat{H}$  is the Hamiltonian governing the system dynamics and  $k$  denotes the so-called Krylov order. The method is meticulously described in Ref. [78], where the authors argue that this strategy is more accurate and more efficient than the two-site TDVP approach. Moreover, this method turns out to be more reliable in the case of beyond-nearest-neighbor interactions. We use the algorithm implementation based on the ITensor library provided by the authors of Ref. [78] under the ITensor/TDVP repository.

The calculations we performed with the time step  $\Delta t = 0.02$  and  $k = 3$ , where the truncation error of each application of  $\hat{H}$  to  $|\Psi\rangle$  and the truncation error controlling diagonalization of the sum of the reduced density matrices were chosen to be equal  $10^{-8}$ . Additionally, we preserve exact unitarity by imposing no truncation during one-site TDVP sweeps. This choice of parameters guarantees a balance between cost and accuracy, when testing in the most demanding  $M = 3$  case. We let the bond dimension  $\chi$  of the time-evolved MPS grow up to predetermined value  $\chi_{\max} = 750$  and switch off the global basis expansion routine when  $\chi_{\max}$  is reached. For convergence analysis, see Appendix E.

In contrast to the  $M = 1$  case, the domain structure is preserved over a couple of trap periods for all the interaction strengths (see Fig. 3). It can be further analyzed through the intercomponent density-density correlation function  $G(x, y; t) = \langle \Psi(t) | \hat{n}_\uparrow(x) \hat{n}_\downarrow(y) | \Psi(t) \rangle / M^2$ , with  $\hat{n}_\sigma(x) = \hat{\psi}_\sigma^\dagger(x) \hat{\psi}_\sigma(x)$ , where  $\hat{\psi}_\sigma(x)$  is a canonical Fermi field operator for spin  $\sigma$  at  $x$ ,  $|\Psi(t)\rangle$  is the time-evolved MPS at time  $t$ , and  $\int G(x, y; t) dx dy = 1$ . In Fig. 5, we compare  $\langle G \rangle(x_\uparrow, x_\downarrow)$  obtained for  $M = 1, 3$  and different finite-range attraction strength  $\gamma_\ell$ , where  $\langle \dots \rangle$  denotes a temporal average over five trap periods. Far from  $\gamma_{\text{crit}}$  both systems evolve similarly, suggesting that mechanisms described in the previous section are present also for  $M > 1$ . On the other hand, in the intermediate regime  $\gamma_\ell \approx \gamma_{\text{crit}}$ , an escalation of  $\langle G \rangle$  at  $|x_\uparrow - x_\downarrow| \approx \ell$  is revealed for  $M = 3$ , alongside a slight flow of atoms to the opposite side of the domain wall. We interpret this enhancement as the onset of the bound state contribution (molecule fraction)

appearing in the course of time evolution. It can be viewed as an extension of similar structures present in the relative wave function of the bound state in the two-body problem (see Appendix B). Additionally, this growth takes place at the critical interaction strength predicted by the LOCV approximation and  $M = 1$  exact solution. Note that for  $M = 1$ , the dynamics reveals no molecular formation as there are no additional atoms to absorb excess kinetic energy.

This effect can be further investigated by analysis of the pair distribution function  $g(r; t) = \int K_r(x; t) dx$ , where  $K_r(x; t) = \frac{1}{2} \sum_{q=\pm} [G(x, x + qr; t) + G(x + qr, x; t)]$  describes spatial correlations between spin- $\uparrow$  and spin- $\downarrow$  fermions at a distance  $r$ . The value of  $g(r; t)$  corresponds to the probability density of finding opposite-spin fermions at a distance  $r$ . A temporal variability of  $g(r; t)$  obtained for  $M = 1, 3$  and different  $\gamma_\ell$  is presented in Figs. 5(k)–5(o). For  $M = 1$ , independently of the  $\gamma_\ell$  value,  $g(r; t)$  oscillates, closely following the dynamics of single-particle densities; cf. Figs. 3(e)–3(f) and upper panels of Figs. 5(k)–5(o). In contrast, for  $\gamma_\ell \approx \gamma_{\text{crit}}$ , the  $M = 3$  case reveals a steady and gradual growth of  $g(r; t)$  at  $r = \ell$ , being the distance at which signatures of anticipated bound pairs are expected. Since the dominant contribution to  $g(\ell; t)$  comes from the trap center, cf. Figs. 5(h) and 5(i), we interpret this result as a footprint of molecular fraction in the interlayer between components. Far from  $\gamma_\ell \approx \gamma_{\text{crit}}$ , the resulting  $g(\ell; t)$  is inappreciable, suggesting that stabilization mechanisms noticed and described in the two-body case are also present in larger systems.

To study the molecular fraction in more detail, one can compute  $\mathcal{N}_{\uparrow\downarrow}^\ell = M g(\ell; t) \ell$  representing the expectation value of the number of  $\uparrow\downarrow$  pairs of size  $\approx \ell$ . Since the components in the initial state are spatially separated, the anticipated  $\uparrow\downarrow$  bound structures may appear in the course of time evolution. Therefore, in Fig. 6(a), we investigate how the temporal average  $\langle \mathcal{N}_{\uparrow\downarrow}^\ell \rangle$  depends on  $M$  and the beyond-contact attraction  $\gamma_\ell$ . It is striking that while  $\langle \mathcal{N}_{\uparrow\downarrow}^\ell \rangle$  turns out to be almost  $M$  independent for  $\gamma_\ell > \gamma_{\text{crit}}$ , at  $\gamma_\ell \approx \gamma_{\text{crit}}$  one observes an abrupt splitting between the results obtained for  $M = 1$  and  $M > 1$ . For both  $M = 2$  and  $M = 3$ ,  $\langle \mathcal{N}_{\uparrow\downarrow}^\ell \rangle$  is very similar and reveals a dramatic growth up to  $\approx 0.2$ . When  $\gamma_\ell$  becomes more negative, it rapidly decays approaching the values obtained for  $M = 1$ . The escalation of  $\langle \mathcal{N}_{\uparrow\downarrow}^\ell \rangle$  for  $M > 1$  around  $\gamma_{\text{crit}}$  can be better understood when looking at the spatial distribution  $\langle K_\ell \rangle(x)$ . That is, as shown for  $M = 3$  in Fig. 6(b), in the vicinity of  $\gamma_{\text{crit}}$  there is a significant accumulation of  $\uparrow\downarrow$  pairs of size  $\ell$  in the center of the trap. This is an additional signature of an appearance of a molecular fraction that resides between the two components forming a domain wall. Coexistence of paired and unpaired fermions has been observed experimentally in a three-dimensional system, where strong evidence of a microscale phase separation was provided [34,36].

## V. CONCLUSIONS

We proposed to utilize the three- $\delta$  interaction potential to study competing effects, intercomponent pairing and ferromagnetism, in an ultracold two-component Fermi gas. We have analyzed many-body dynamics of the system initially prepared in the experimentally inspired artificial domain

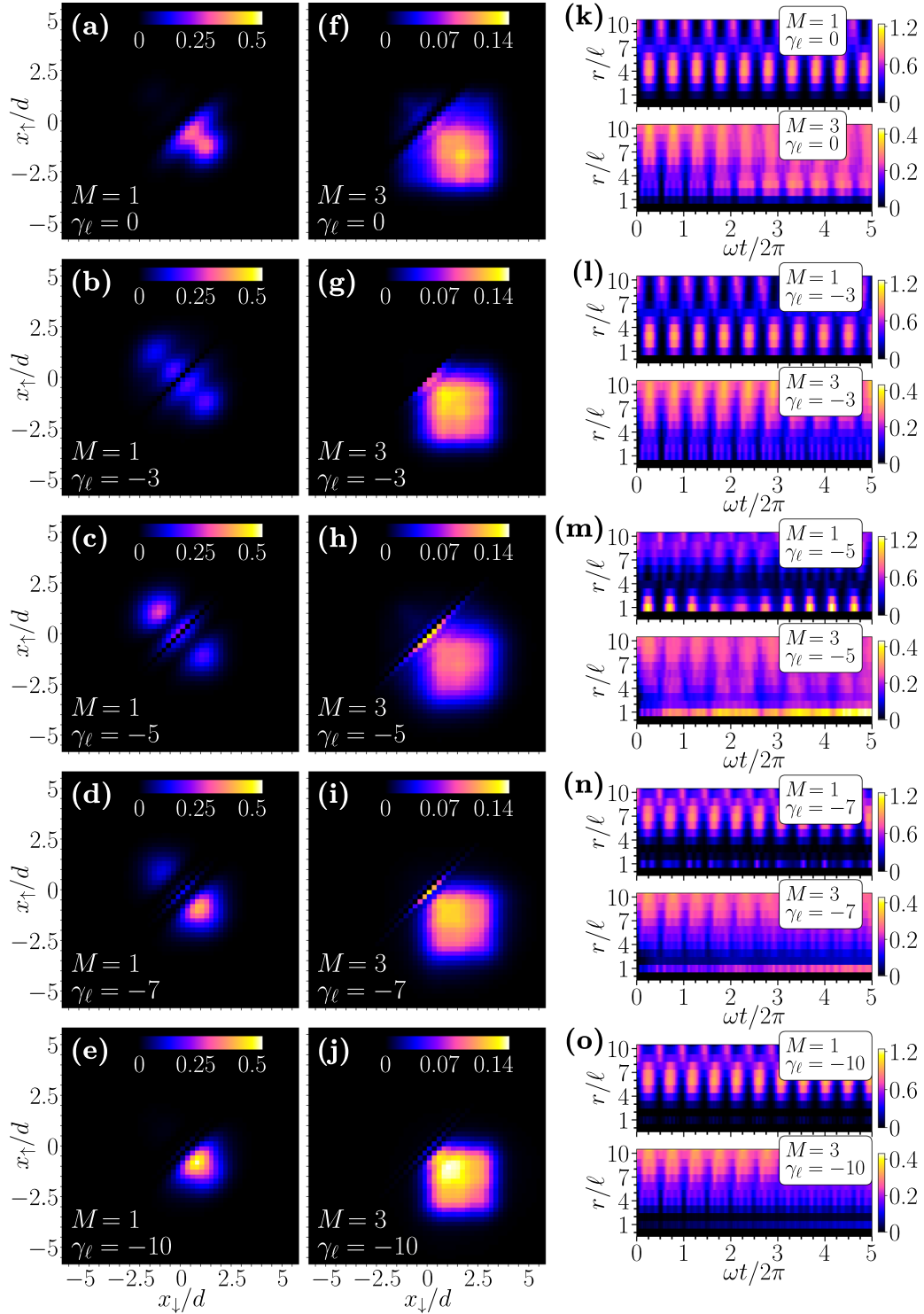


FIG. 5. Temporally averaged over five trap periods density-density correlation functions  $\langle G(x_{\uparrow}, x_{\downarrow}) \rangle$  calculated for  $M = 1$ , panels (a)–(e), and  $M = 3$ , panels (f)–(j), and for different finite-range attraction strengths  $\gamma_{\ell}$ . In accordance with the results shown in Fig. 3, mixing between the components takes place only for  $M = 1$  in the presence of intermediate attraction; see panels (b)–(d). In contrast to the  $M = 1$  case, for  $M = 3$  with moderate attraction one can observe an accumulation of  $\langle G(x_{\uparrow}, x_{\downarrow}) \rangle$  in the trap center; see panels (g)–(i). In right panels (k)–(o), we show a temporal behavior of  $g(r; t)$  obtained for  $M = 1, 3$  and different  $\gamma_{\ell}$ . While for  $M = 1$  the pair distribution  $g(r; t)$  oscillates together with single-particle densities plotted in Fig. 3(d)–3(f), for  $\gamma_{\ell} \approx \gamma_{\text{crit}}$  the  $M = 3$  case reveals a steady and gradual increase of correlations between opposite-spin fermions separated by  $r \approx \ell$ . Such correlations are strictly related to the presence of the finite-range attraction.

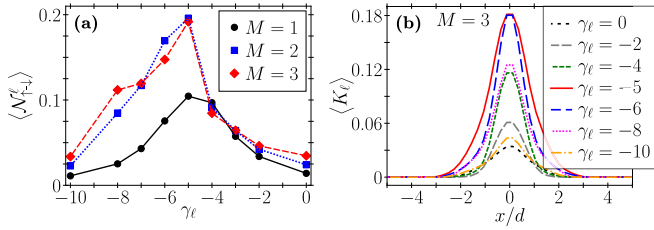


FIG. 6. Panel (a) shows the expectation value of the number of molecules  $\langle \mathcal{N}_{\uparrow\downarrow}^\ell \rangle$  averaged over five trap periods vs finite-range attraction strength  $\gamma_\ell$ . The results obtained for  $M = 2$  and  $M = 3$  are very similar and reveal a dramatic growth of  $\uparrow\downarrow$  pair correlations at a distance  $r \approx \ell$  for  $\gamma_\ell \approx -5$ . On the other hand, for  $M = 1$ , an increase of  $\langle \mathcal{N}_{\uparrow\downarrow}^\ell \rangle$  is much less pronounced, which may indicate lack of the molecule formation in the two-body system. Panel (b) presents the  $M = 3$  case of  $\langle K_\ell \rangle(x)$  determined for different beyond-contact attraction strengths  $\gamma_\ell$ . The correlations are significantly amplified for  $\gamma_\ell \approx \gamma_{\text{crit}} = -5$  and reveal maximum in the trap center, suggesting that the molecular fraction accumulates between two Fermi clouds.

structure. We have found that the formation of molecules does not immediately destroy the phase separation within the considered timescales of several trap periods. Instead, the molecular fraction accumulates between the components, coexisting with unpaired fermions. Moreover, the simple model we consider should be realizable in optical lattices with ultracold atoms.

#### ACKNOWLEDGMENTS

The authors would like to thank Titas Chanda, Krzysztof Jachymski, and Vicky C. Arizona for fruitful discussions. A.S. acknowledges the support from Olle Engkvists stiftelse. M.Ł. acknowledges the support from the (Polish) National Science Center Grant No. 2018/31/N/ST2/01429. P.T.G. is financed from the (Polish) National Science Center Grants No. 2018/29/B/ST2/01308 and No. 2020/36/T/ST2/00065. K.R. is supported by the (Polish) National Science Center Grant No. 2018/29/B/ST2/01308. Center for Theoretical Physics of the Polish Academy of Sciences is a member of the National Laboratory of Atomic, Molecular, and Optical Physics (KL FAMO).

#### APPENDIX A: BOUND STATES IN TWO-BODY PROBLEM

In this Appendix, we investigate a one-dimensional problem of two particles interacting via a three- $\delta$  potential and determine a criterion for a bound-state formation in the absence of external confinement. The Hamiltonian of our system reads

$$H = -\frac{\hbar^2}{2m}(\partial_x^2 + \partial_y^2) + W_{\uparrow\downarrow}(x-y) \quad (\text{A1})$$

with  $W_{\uparrow\downarrow}(x) = c_0\delta(x) + c_\ell\delta(x-\ell) + c_\ell\delta(x+\ell)$  and we assume that  $c_0 > 0$  and  $c_\ell < 0$ . We decouple center of mass (c.m.) and relative motion by introducing new coordinates  $R = (x+y)/\sqrt{2}$  and  $r = (x-y)/\sqrt{2}$  obtaining  $H = H_{\text{c.m.}} + H_{\text{rel}}$ , where  $H_{\text{c.m.}} = -\frac{\hbar^2}{2m}\partial_R^2$  and  $H_{\text{rel}} = -\frac{\hbar^2}{2m}\partial_r^2 + W'(r)$ . Here  $W'(r)$  denotes the three- $\delta$  potential with  $\ell' = \ell/\sqrt{2}$  and  $c'_{0,\ell} =$

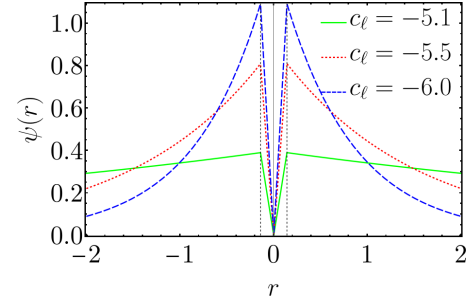


FIG. 7. Bound state relative wave functions of the three- $\delta$  potential in the regime of strong contact repulsion. Note that with increasing  $|c_\ell|$  the particles localize more eagerly at  $r = \pm\ell'$  (marked with dashed lines). The relative wave functions vanish at  $r = 0$  due to the strong pointlike repulsion. Results were obtained for  $\hbar = m = 1$ ,  $c_0 = 5000$ , and  $\ell = 0.2$ .

$c_{0,\ell}/\sqrt{2}$ . We focus on  $H_{\text{rel}}$  and seek for localized eigenstates (bound states) describing a pair bound due to attractive part of  $W'(r)$ . In general, the potential may have at most two bound states: one symmetric (+) and one antisymmetric (-). The problem is solved by imposing the following standard continuity and  $\delta$ -potential-related conditions

$$\psi_{\pm}(r) = \begin{cases} A_{\pm}e^{kr} & r < -\ell' \\ B_{\pm}e^{kr} + C_{\pm}e^{-kr} & -\ell' \leq r < 0 \\ \pm C_{\pm}e^{kr} \pm B_{\pm}e^{-kr} & 0 \leq r < \ell' \\ \pm A_{\pm}e^{-kr} & r \geq \ell' \end{cases}, \quad (\text{A2})$$

where  $k = \sqrt{2m|E|}/\hbar$ , with  $E$  being the binding energy. The above-mentioned conditions lead to the following relations,  $B_+ = C_+(2 - u_0/t)/(2 + u_0/t)$ ,  $A_+ = -2C_+t e^{2t}/u_\ell$  for symmetric solutions and  $B_- = -C_-$ ,  $A_- = -2C_-t e^{2t}/u_\ell$  for antisymmetric ones, where the dimensionless parameters  $u_0 = mc_0\ell/\hbar^2$ ,  $u_\ell = mc_\ell\ell/\hbar^2$ , and  $t = k\ell'$  were introduced. The energies  $E$  can be determined thanks to relations

$$\begin{cases} 2 \cosh t + \frac{u_0}{t} \sinh t + (2t + u_0) \frac{e^t}{u_\ell} = 0 & \text{for } (+) \\ t e^t = -u_\ell \sinh t & \text{for } (-) \end{cases}. \quad (\text{A3})$$

As the lowest energy state is always symmetric, our potential hosts a bound state only if (A3) has a positive solution. Assuming a very strong contact repulsion  $c_0 \rightarrow \infty$ , we take the limit  $t \rightarrow 0^+$  in (A3) and find the critical value of attractive coupling  $u_\ell^{\text{crit}} = -1$  below which there exists a bound state in the system. While the regime of bound-state existence is shown in Fig. 1, exemplary shapes of the corresponding bound-state wave functions can be found in Fig. 7.

#### APPENDIX B: TWO-BODY PROBLEM IN A HARMONIC TRAP

Let us now study the problem of two initially separated particles interacting via three- $\delta$  potential. We show that exact solutions provide us with a lot of insights about the time evolution and the structure of the energy spectrum. Additionally, it will serve as a benchmark for numerical methods employed when investigating larger systems.

Here, applying methods similar to those in Refs. [71,85], we solve the problem that may be viewed as an extension of

the problem analyzed in Ref. [71]. Namely, we consider the Hamiltonian

$$H = -\frac{\hbar^2}{2m}(\partial_x^2 + \partial_y^2) + \frac{1}{2}m\omega^2(x^2 + y^2) + W_{\uparrow\downarrow}(x - y). \tag{B1}$$

As in the previous section, we introduce  $R$  and  $r$  variables obtaining  $H = H_{c.m.} + H_{rel}$ , where  $H_{c.m.}$  describes the standard Hamiltonian of harmonic oscillator and thus we focus only on  $H_{rel} = -\frac{\hbar^2}{2m}\partial_r^2 + \frac{m\omega^2}{2}r^2 + W'(r)$ . In the absence of potential  $W'(r)$ , the corresponding Schrödinger equation describes a standard harmonic oscillator in 1D, i.e.,  $E\psi(r) = -\frac{\hbar^2}{2m}\partial_r^2\psi(r) + \frac{m\omega^2}{2}r^2\psi(r)$ . The most general solutions of the problem can be grouped into symmetric and antisymmetric ones and cast into the following forms:

$$\psi_+(r) = \alpha_+\tilde{F}_{\frac{\sigma}{2}, \frac{1}{2}}(r) + \beta_+\tilde{U}_{\frac{\sigma}{2}, \frac{1}{2}}(r), \tag{B2}$$

$$\psi_-(r) = \alpha_-\tilde{F}_{\frac{\kappa}{2}, \frac{3}{2}}(r) + \beta_-\tilde{U}_{\frac{\kappa}{2}, \frac{3}{2}}(r), \tag{B3}$$

where  $d = \sqrt{\hbar/m\omega}$  is the oscillator length and the energy-related coefficients  $\kappa = 3/2 - E/\hbar\omega$  and  $\sigma = 1/2 - E/\hbar\omega$  [85,86]. Additionally, for convenience we introduced functions  $\tilde{F}_{\xi, \zeta}(r) = \exp(-r^2/2d^2) {}_1F_1(\xi; \zeta; r^2/d^2)$  and  $\tilde{U}_{\xi, \zeta}(r) = \exp(-r^2/2d^2)U(\xi, \zeta, r^2/d^2)$ , where  $U$  and  ${}_1F_1$  are confluent hypergeometric functions of the first and second types, respectively. It is important for further analysis to list the most important properties of  ${}_1F_1$  and  $U$  in order to construct physical eigenstates (taking  $\delta$  functions into the account) similarly to the case without confinement [85,86]. If  $\sigma = -n$  with  $n = 0, 1, 2, \dots$ , then  ${}_1F_1(-\frac{n}{2}; \frac{1}{2}; x^2) \sim H_{2n}(x)$  and for  $\kappa = -n$  ( $n = 0, 1, 2, \dots$ ) we get  ${}_1F_1(-\frac{n}{2}; \frac{3}{2}; x^2) \sim H_{2n+1}(x)$ . In this way, we retrieve free oscillator solutions out of general forms (B2) and (B3). However, when interactions shift values of energies so that  $\sigma$  and  $\kappa$  are no longer nonpositive integer numbers, the functions  $\tilde{F}_{\frac{\sigma}{2}, \frac{1}{2}}(r)$  and  $\tilde{F}_{\frac{\kappa}{2}, \frac{3}{2}}(r)$  become non-normalizable. This means that in the region where  $|r| > \ell'$  we have solutions with  $\alpha^{(+)} = 0$  ( $\alpha^{(-)} = 0$ ) in the symmetric (antisymmetric) case. On the other hand, in that case functions  $\tilde{U}_{\frac{\sigma}{2}, \frac{1}{2}}(r)$  and  $\tilde{U}_{\frac{\kappa}{2}, \frac{3}{2}}(r)$  de-

cay sufficiently quickly, assuring normalizability of the wave function. Now, regarding behavior of the wave functions at the origin, functions  $\tilde{F}_{\frac{\sigma}{2}, \frac{1}{2}}(r)$  and  $\tilde{F}_{\frac{\kappa}{2}, \frac{3}{2}}(r)$  are continuous and have continuous derivatives at  $r = 0$ . The situation is slightly different for  $\tilde{U}_{\frac{\sigma}{2}, \frac{1}{2}}(r)$  and  $\tilde{U}_{\frac{\kappa}{2}, \frac{3}{2}}(r)$ , which are continuous at  $r = 0$  but reveal discontinuities in derivatives at this point, which we use to fulfill the abovementioned Dirac  $\delta$  conditions. These properties motivate us to propose solutions in the form

$$\psi_+(r) = \begin{cases} A_+\tilde{U}_{\frac{\sigma}{2}, \frac{1}{2}}(r) & |r| \geq \ell' \\ B_+\tilde{F}_{\frac{\sigma}{2}, \frac{1}{2}}(r) + C_+\tilde{U}_{\frac{\sigma}{2}, \frac{1}{2}}(r) & |r| < \ell' \end{cases}, \tag{B4}$$

$$\psi_-(r) = \begin{cases} A_-\tilde{U}_{\frac{\kappa}{2}, \frac{3}{2}}(r) & |r| \geq \ell' \\ B_-\tilde{F}_{\frac{\kappa}{2}, \frac{3}{2}}(r) & |r| < \ell' \end{cases}. \tag{B5}$$

Now, we proceed similarly as in the case with no confinement; i.e., we impose continuity and  $\delta$ -potential-related conditions at  $r = 0, \pm\ell'$ . Let us start with the symmetric solutions, where continuity of the wave function at  $r = \pm\ell'$  implies

$$A_+U\left(\frac{\sigma}{2}, \frac{1}{2}, \frac{\ell'^2}{d^2}\right) = B_+{}_1F_1\left(\frac{\sigma}{2}; \frac{1}{2}; \frac{\ell'^2}{d^2}\right) + C_+U\left(\frac{\sigma}{2}, \frac{1}{2}, \frac{\ell'^2}{d^2}\right) \tag{B6}$$

and  $\delta$ -induced condition at  $r = 0$  yields (see Ref. [86] for details)

$$C_+\hbar\omega d \frac{\sqrt{\pi}\sigma}{\Gamma(1 + \frac{\sigma}{2})} + c'_0\left[B_+ + C_+\frac{\sqrt{\pi}}{\Gamma(\frac{1}{2} + \frac{\sigma}{2})}\right] = 0. \tag{B7}$$

Applying the same conditions but at  $r = \pm\ell$  together with relations (B6) and (B7), one finds

$$B_+ = -\Xi_\sigma C_+, \tag{B8}$$

$$A_+ = \frac{2\Xi_\sigma {}_1F_1\left(1 + \frac{\sigma}{2}; \frac{3}{2}; \frac{\ell'^2}{d^2}\right) + U\left(1 + \frac{\sigma}{2}, \frac{3}{2}, \frac{\ell'^2}{d^2}\right)}{U\left(1 + \frac{\sigma}{2}, \frac{3}{2}, \frac{\ell'^2}{d^2}\right) - 2\frac{c'_0}{\hbar\omega\ell'\sigma}U\left(\frac{\sigma}{2}, \frac{1}{2}, \frac{\ell'^2}{d^2}\right)}C_+, \tag{B9}$$

where  $\Xi_\sigma = \sqrt{\pi}[\hbar\omega d\sigma/c'_0\Gamma(1 + \frac{\sigma}{2}) + 1/\Gamma(\frac{1}{2} + \frac{\sigma}{2})]$  was introduced for convenience. By plugging these equalities into the continuity condition, we determine the equation for  $\sigma$  (directly related to energies)

$$\frac{\sigma U\left(\frac{\sigma}{2}, \frac{1}{2}, \frac{\ell'^2}{d^2}\right)}{U\left(\frac{\sigma}{2}, \frac{1}{2}, \frac{\ell'^2}{d^2}\right) - \Xi_\sigma {}_1F_1\left(\frac{\sigma}{2}; \frac{1}{2}; \frac{\ell'^2}{d^2}\right)} = \frac{\sigma U\left(1 + \frac{\sigma}{2}, \frac{3}{2}, \frac{\ell'^2}{d^2}\right) + \frac{2c'_0}{\hbar\omega\ell'\sigma}U\left(\frac{\sigma}{2}, \frac{1}{2}, \frac{\ell'^2}{d^2}\right)}{2\Xi_\sigma {}_1F_1\left(1 + \frac{\sigma}{2}; \frac{3}{2}; \frac{\ell'^2}{d^2}\right) + U\left(1 + \frac{\sigma}{2}, \frac{3}{2}, \frac{\ell'^2}{d^2}\right)}. \tag{B10}$$

When dealing with antisymmetric solutions, the corresponding wave functions are not affected by the  $\delta$  potential at  $r = 0$  and thus it is enough to focus on  $r = \pm\ell'$  cases, where from the continuity and  $\delta$ -related conditions we find

$$A_-U\left(\frac{\kappa}{2}, \frac{3}{2}, \frac{\ell'^2}{d^2}\right) = B_-{}_1F_1\left(\frac{\kappa}{2}; \frac{3}{2}; \frac{\ell'^2}{d^2}\right), \tag{B11}$$

$$A_- = -\frac{\kappa\left[\frac{A_-}{2}U\left(1 + \frac{\kappa}{2}, \frac{5}{2}, \frac{\ell'^2}{d^2}\right) + \frac{B_-}{3}{}_1F_1\left(1 + \frac{\kappa}{2}; \frac{5}{2}; \frac{\ell'^2}{d^2}\right)\right]}{c'_0U\left(\frac{\kappa}{2}, \frac{3}{2}, \frac{\ell'^2}{d^2}\right)}. \tag{B12}$$

Finally,  $\kappa$  gives the energies of antisymmetric states and can be determined from

$$-\kappa = \frac{\frac{2c'_\ell}{\hbar\omega\ell'} U\left(\frac{\kappa}{2}, \frac{3}{2}, \frac{\ell'^2}{d^2}\right) {}_1F_1\left(\frac{\kappa}{2}; \frac{3}{2}; \frac{\ell'^2}{d^2}\right)}{{}_1F_1\left(\frac{\kappa}{2}; \frac{3}{2}; \frac{\ell'^2}{d^2}\right) U\left(1 + \frac{\kappa}{2}, \frac{5}{2}, \frac{\ell'^2}{d^2}\right) + \frac{2}{3} U\left(\frac{\kappa}{2}, \frac{3}{2}, \frac{\ell'^2}{d^2}\right) {}_1F_1\left(1 + \frac{\kappa}{2}; \frac{5}{2}; \frac{\ell'^2}{d^2}\right)}. \quad (\text{B13})$$

Our eigenproblem is now solved. Energies are readily obtained as numerical solutions of (B10) and (B13). Wave functions are determined from Eqs. (B8), (B9), and (B11) together with the normalization condition. Ground states for different parameters are presented in Fig. 8. In summary, let us note that full eigenstates of the two body problem can be cast into the following form

$$\Psi_{n,\mu}(x, y) = \phi_n\left(\frac{x+y}{\sqrt{2}}\right) \psi_\mu\left(\frac{x-y}{\sqrt{2}}\right), \quad (\text{B14})$$

where  $\phi_n$ ,  $n = 0, 1, 2, \dots$  is a harmonic oscillator eigenstate whereas  $\psi_\mu$  represents an eigenstate of  $H_{\text{rel}}$ . Here  $\mu$  denotes either  $\kappa$  or  $\sigma$  depending on the symmetry of a given state in the relative coordinate  $r$ .

### APPENDIX C: THREE- $\delta$ POTENTIAL IN LOC V APPROXIMATION

We consider a specific potential consisting of three  $\delta$  contributions

$$W_{\uparrow\downarrow}(x) = c_0\delta(x) + c_\ell\delta(x - \ell) + c_\ell\delta(x + \ell), \quad (\text{C1})$$

where we choose the contact interaction strength  $c_0$  to be large and positive to mimic the repulsive core of realistic interparticle potential. On the other hand, beyond-contact part,  $c_\ell$ , is chosen to be small and negative to support a weakly bound state and provide the simplest extension of a contact part toward full van der Waals forces.

In a three-dimensional two-component Fermi mixture, the contact repulsion given by the Fermi-Huang pseudopotential  $\propto \delta(r) \frac{\partial}{\partial r} r$  reproduces both the weakly bound pairs (attractive branch of the many-body system) and the repulsive, anticorrelated, phase-separated Fermi clouds (repulsive branch). This is not the case in a one-dimensional space as repulsive contact interactions do not support a bound state.

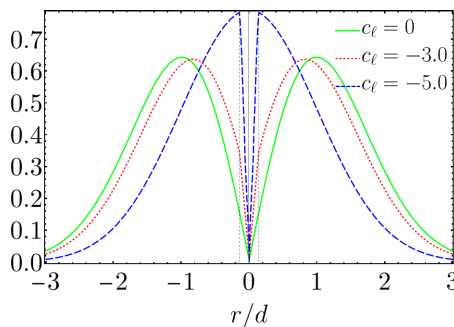


FIG. 8. Ground states of the relative Hamiltonian  $H_{\text{rel}}$  for  $\ell/d = 0.2$ ,  $c_0/\hbar\omega d = 200$ , and different  $c_\ell$ . Similarly to the case without confinement, the solution becomes more localized at  $r = \pm \ell'$  as we increase  $|c_\ell|$ .

To simplify our considerations, we will work in the regime of infinite repulsion,  $c_0 \rightarrow \infty$ , yielding  $f(0) = 0$ .

We compute the interaction energy within the LOC V approximation solving Eqs. (9). If the bound state is considered,  $\lambda = -\hbar^2\kappa^2/2m$  is negative. Then, we assume the Jastrow function to take form

$$f(x) = \begin{cases} A \sinh(\kappa x) & : x \in [0, \ell] \\ B \sinh(\kappa x) + D \cosh(\kappa x) & : x \in (\ell, d] \\ 1 & : x > d, \end{cases} \quad (\text{C2})$$

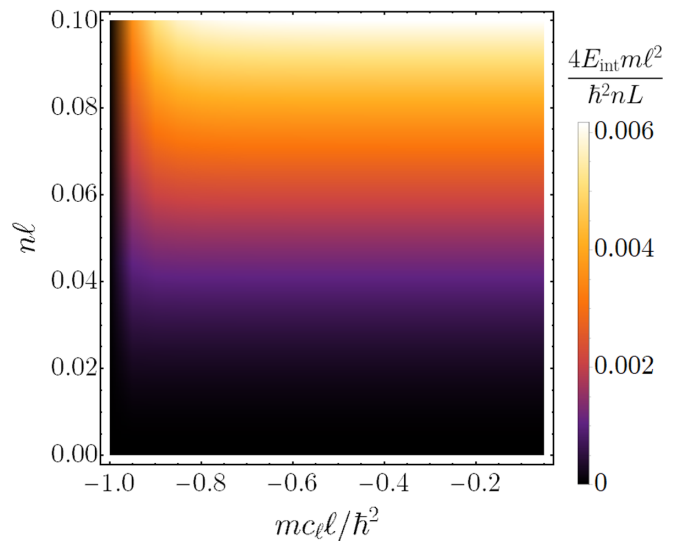
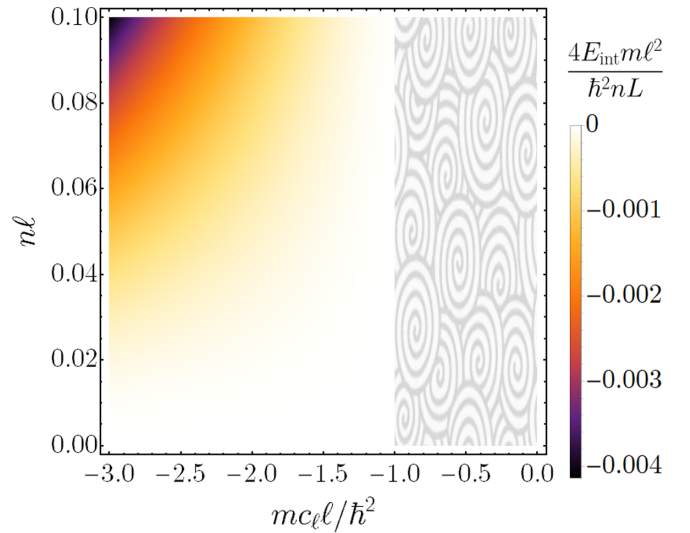


FIG. 9. Interaction energy at the attractive (top panel) and the repulsive (bottom panel) branch of the many-body spectrum with the three- $\delta$  potential within the LOC V approximation as a function of  $n\ell$  and  $mc_\ell\ell/\hbar^2$ . The bound state is supported only when  $mc_\ell\ell/\hbar^2 \lesssim -1$ .

and needs to be self-consistently solved for  $A, B, D, d, \kappa$  with LOCV constraints introduced in the main text. It simplifies to the following two equations,

$$\frac{2}{na} = \cosh^2(\kappa_1 - \kappa_2) \left[ \frac{\coth(\kappa_1)}{\kappa_1} - \operatorname{csch}^2(\kappa_1) \right] + \frac{1}{2\kappa_1} [2\kappa_2 - 2\kappa_1 + \sinh(2\kappa_2 - 2\kappa_1)], \quad (\text{C3})$$

$$\tanh(\kappa_2) = \frac{1}{\tanh(\kappa_1)} + \frac{\kappa_1}{\lambda_2} \frac{1}{\sinh^2(2\kappa_1)}, \quad (\text{C4})$$

where we define  $\kappa_1 = \kappa\ell$ ,  $\kappa_2 = \kappa d$ ,  $\lambda_2 = mc_\ell\ell/\hbar^2$ . The interaction energy density then equals

$$\frac{E_{\text{int}}}{V} = \frac{n}{2}\lambda = -\frac{n}{2} \frac{\hbar^2 \kappa_1^2}{2m\ell^2}. \quad (\text{C5})$$

It is evaluated numerically and presented in Fig. 9(left).

Note that the bound state is not supported for every value of  $c_\ell$ . Most notably, numerical evaluation allows us to write down the simple expression for the existence of the bound state

$$c_\ell \lesssim -\frac{\hbar^2}{m\ell}, \quad (\text{C6})$$

which does not depend on the gas density.

On the other hand, similar procedure for the first excited state (the repulsive branch) yields

$$\frac{2}{na} = [k_1 - \sin(k_1) \cos(k_1)][\cos(k_2) \cot(k_1) + \sin(k_2)]^2 + \frac{1}{2k_1} [2k_2 - 2k_1 + \sin(2k_2 - 2k_1)], \quad (\text{C7})$$

$$\tan(k_2) = -\left[ \frac{1}{\tan(k_1)} + \frac{k_1}{\lambda_2} \frac{1}{\sin^2(2k_1)} \right], \quad (\text{C8})$$

where  $\lambda = \frac{\hbar^2 k^2}{2m}$  is positive and we define  $k_1 = k\ell$ ,  $k_2 = kd$ ,  $\lambda_2 = mc_\ell\ell/\hbar^2$ . The result is presented in Fig. 9(right).

The lowest energy branch of positive solutions to the constrained equations tends to 0 at  $mc_\ell\ell/\hbar^2 \approx -1$ , i.e., the interaction strength at which the bound state starts to be supported. In Fig. 2, the energy dependence on parameter  $c_\ell$  for the many-body ground state at a given density is presented. The sharp transition is clearly visible, suggesting nontrivial behavior of the system at the critical value of  $c_\ell$ .

## APPENDIX D: SHORT-RANGE ATOMIC POTENTIALS

### 1. Scattering in quasi-one-dimensional geometry

Here we sum up the analysis of Ref. [54], where the authors show how finite-range corrections to the standard pointlike  $\delta$  interaction can be modeled through the effective pseudopotential

$$W_p(x) = g_{1D}(1 + g'p^2)\delta(x), \quad (\text{D1})$$

where  $g_{1D}$  denotes a one-dimensional mean field interaction strength,  $g'$  is a parameter depending on the details of the physical situation, and following Ref. [54],  $\hbar p$  represents a one-dimensional momentum operator.

The system under consideration involves ultracold atoms interacting via the attractive part of the van der Waals po-

tential  $W_{\text{vdW}}(r) = -C_6/r^6$  with a characteristic length (mean scattering length)  $\bar{a} = \frac{2\pi}{\Gamma(1/4)^2} (2\mu C_6/\hbar^2)^{1/4}$ , where  $\mu$  is the reduced mass of the atomic pair [87] and  $\Gamma$  is the Euler  $\gamma$  function. It can be rephrased in terms of the van der Waals radius  $R_{\text{vdW}}$  as  $\bar{a} = 0.955978R_{\text{vdW}}$ .

In the presence of tight harmonic confinement  $\frac{1}{2}\mu\omega^2\rho^2$   $\rho = \sqrt{y^2 + z^2}$  and  $\omega$  denotes trapping frequency, the usual Fermi-Huang pseudopotential can be generalized to account for an energy dependence

$$W_{\text{FH}}(\mathbf{r}) = -\frac{2\pi\hbar^2}{\mu} \frac{\tan \delta_{3D}(k)}{k} \delta(\mathbf{r}) \frac{\partial}{\partial r} r, \quad (\text{D2})$$

where  $\hbar^2 k^2/2\mu$  is the kinetic energy of the relative motion and  $\delta_{3D}(k)$  is the phase shift due to interactions. Consequently, the corresponding energy-dependent scattering length reads  $a_{3D}(k) = -\tan \delta_{3D}(k)/k$ .

One notes that the full three-dimensional scattering analysis can be reduced to the 1D problem in the  $s$ -wave channel with the pseudopotential [54,88–91]

$$W_{1D} = g_{1D}(p)\delta(x), \quad (\text{D3})$$

where

$$g_{1D}(p) = -\frac{\hbar^2}{\mu} p \tan [\delta_{1D}(p)]. \quad (\text{D4})$$

Here,  $\delta_{1D}(p)$  is a 1D phase shift depending on 1D momentum  $\hbar p$ , where  $k^2 = p^2 + 2/d_\perp^2$  with  $d_\perp = \sqrt{\hbar/\mu\omega}$ .

Expanding (D4) in small  $p$  up to the second order, one finds

$$g_{1D}(p) \approx g_{1D}(1 + g'p^2), \quad (\text{D5})$$

with

$$\frac{\mu}{\hbar^2} g_{1D} = \frac{2}{d_\perp} \left( \frac{d_\perp}{a_{3D}} - C - \frac{r_{3D}}{d_\perp} \right)^{-1}, \quad (\text{D6})$$

$$g' = \frac{d_\perp}{2} \frac{r_{3D} - \tilde{C}d_\perp}{\frac{d_\perp}{a_{3D}} - C - \frac{r_{3D}}{d_\perp}}, \quad (\text{D7})$$

where  $\tilde{C} = \zeta(3/2)/8 \approx 0.3265$  and  $C = -\zeta(1/2) \approx 1.46035$ . The effective range  $r_{3D}$  can be determined from the expansion

$$k \cot [\delta_{3D}(k)] = -\frac{1}{a_{3D}} + \frac{1}{2} r_{3D} k^2 + O(k^2). \quad (\text{D8})$$

In vicinity of the Feshbach resonance, the effective range of a single-channel van der Waals potential can be determined analytically [92–94],

$$r_{3D} = \frac{\Gamma(1/4)^4 \bar{a}}{6\pi^2} \left( 1 - \frac{2\bar{a}}{a_{3D}} + \frac{2\bar{a}^2}{a_{3D}^2} \right) - 2R_* \left( 1 - \frac{a_{\text{bg}}}{a_{3D}} \right)^2, \quad (\text{D9})$$

where  $R_* = \hbar^2/(2\mu a_{\text{bg}} \Delta \delta\mu)$ ,  $a_{\text{bg}}$  is the background scattering length away from the resonance,  $\Delta$  denotes the resonance width, and  $\delta\mu$  is the magnetic moment difference between channels. This expression approximately holds for open channels, but can fail in the presence of the closed ones [94]. Then, it is more accurate to use formula

$$r_{3D}(B) \approx \frac{v + r_0[a_{3D}(B) - a_{\text{ex}}]^2}{a_{3D}(B)^2}, \quad (\text{D10})$$

where the magnetic field dependence of  $a_{3D}$  reads

$$a_{3D}(B) = a_{bg} \left( 1 - \frac{\Delta}{B - B_0} \right), \quad (\text{D11})$$

with  $B_0$  being the resonance point, and the fitting parameters  $v$ ,  $r_0$ , and  $a_{ex}$  depend on a particular resonance and can be evaluated through the numerical solutions of a full multichannel Schrödinger equation.

## 2. Mapping onto three- $\delta$ potential

We will now proceed to discretize effective interaction potential (D1). The starting point is to consider two-body problem with a total wave function

$$\Psi_f(x, y) = \Psi_R(R)\Psi(r), \quad (\text{D12})$$

where  $R = x + y$  describes the decoupled center-of-mass motion of two atoms,  $r = x - y$  describes the relative motion, and  $x, y$  represent positions of atoms. For the  $\delta$  interaction  $W_a(x - y) = g\delta(x - y - a)$ , the interaction energy reads

$$E = \int dx dy \Psi_f^*(x, y) W_a(x - y) \Psi_f(x, y) = \frac{g}{2} |\Psi(a)|^2. \quad (\text{D13})$$

The position representation of potential (D1) can be written as

$$W_p(x) = g_{1D} \left[ \delta(x) + \frac{g'}{2} \left( \overleftarrow{\partial}_x^2 \delta(x) + \delta(x) \overrightarrow{\partial}_x^2 \right) \right]. \quad (\text{D14})$$

After discretizing the second derivative, i.e.,  $f''(x) \approx [f(x + \Delta x) + f(x - \Delta x) - 2f(x)](\Delta x)^{-2}$ , the energy associated with the last term of the sum in (D14) reads

$$E = -\frac{g_{1D}g'}{4(\Delta x)^2} \int dx [\Psi^*(x + \Delta x) + \Psi^*(x - \Delta x) - 2\Psi^*(x)] \delta(x) \Psi(x). \quad (\text{D15})$$

After realizing that

$$\begin{aligned} & \frac{1}{2} [\Psi^*(x + \Delta x) \Psi(x) + \Psi(x + \Delta x) \Psi^*(x)] \\ &= \Psi^*(x + \Delta x) \Psi(x + \Delta x) + O((\Delta x)^2), \end{aligned} \quad (\text{D16})$$

one finds the interaction energy related to the finite-range correction

$$E = -\frac{g_{1D}g'}{2(\Delta x)^2} \left[ \left| \Psi\left(\frac{\Delta x}{2}\right) \right|^2 + \left| \Psi\left(-\frac{\Delta x}{2}\right) \right|^2 - 2|\Psi(0)|^2 \right]. \quad (\text{D17})$$

By Eq. (D13), it corresponds to the following potential,

$$W_b(x) = -\frac{g_{1D}g'}{(\Delta x)^2} \left[ \delta\left(x + \frac{\Delta x}{2}\right) + \delta\left(x - \frac{\Delta x}{2}\right) - 2\delta(x) \right], \quad (\text{D18})$$

where  $\Delta x$  can be arbitrarily chosen. It is convenient to denote  $\Delta = \sqrt{|g'|}/\alpha$  with some arbitrary real number  $\alpha > 0$ . As a result, we reproduce the three- $\delta$  potential

$$W_{\uparrow\downarrow}(x) = c_0\delta(x) + c_\ell\delta(x - \ell) + c_\ell\delta(x + \ell), \quad (\text{D19})$$

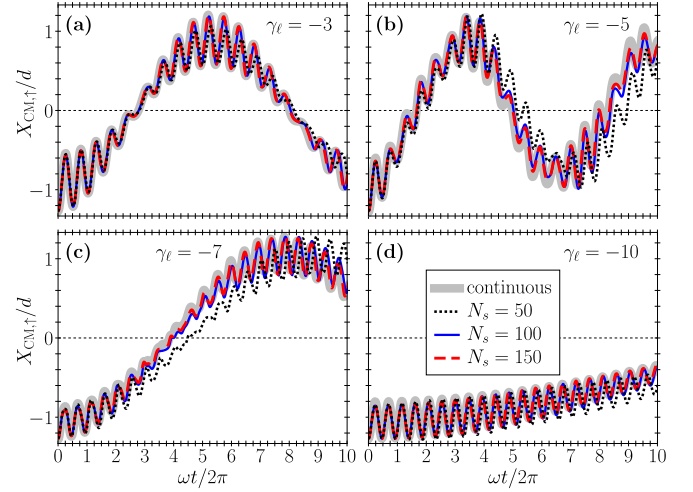


FIG. 10. Comparison between dynamics of the center of mass of the spin- $\uparrow$  component obtained in continuous and discretized models with  $M = 1$ , different number of sites  $N_s = 50, 100, 150$ , and different beyond contact attraction  $\gamma_\ell = -3, -5, -7, -10$ .

with

$$\begin{cases} c_0 = (1 + 2\alpha^2 \operatorname{sgn} g') g_{1D} \\ c_\ell = -\alpha^2 \operatorname{sgn} g' g_{1D} \\ \ell = \sqrt{|g'|}/2\alpha \end{cases}, \quad (\text{D20})$$

and inversely  $g_{1D} = c_0 + 2c_\ell$ ,  $g' = -4\ell^2 c_\ell / (c_0 + 2c_\ell)$ .

Note that  $g'$  and  $g_{1D}$  can be uniquely determined by  $c_0$ ,  $c_\ell$ , and  $\ell$ , while  $\alpha$  provides additional information on how to perform inverse transformation. It is due to the fact that  $g'$  and  $g_{1D}$  describe only the scattering properties of the physical system. Effectively,  $\alpha$  fine-tunes the length scale introduced through the equality  $\ell = \sqrt{|g'|}/2\alpha$  and can be evaluated by considering other properties of the two-body problem, such as the bound-state energy.

## APPENDIX E: CONVERGENCE ANALYSIS

First, we benchmark obtained results in the  $M = 1$  case, where the exact results in the continuous space are known. Namely, we consider the system with different numbers of sites  $N_s = 50, 100, 150$ , but with the same  $\ell = 0.2$  in the three- $\delta$   $W_{\uparrow\downarrow}(x)$  potential, Eq. (1). Since  $\Delta = L/N_s$ , in order to compare the numerical results with the analytical predictions, it is required to take into account different beyond-contact attraction term in the discretized space, i.e., different values of the integer  $s$  in the Hamiltonian (14). That is, while for  $N_s = 50$  we employ nearest neighbor attraction ( $s = 1$ ), for  $N_s = 100$  and  $N_s = 150$  we incorporate next to nearest neighbor ( $s = 2$ ) and second next to nearest neighbor ( $s = 3$ ) interactions, respectively. The comparison between dynamics of the center-of-mass position of  $\uparrow$ -component,  $X_{c.m.,\uparrow}$ , determined analytically in the continuous model and numerically in the discretized system for  $\gamma_\ell = -3, -5, -7, -10$  is illustrated in Fig. 10. Note that the results obtained for  $N_s = 100$  and  $N_s = 150$  are almost identical to the analytical ones, showing the convergence and reliability of the TDVP evolution we employed. On the other hand, in the case of  $N_s = 50$  the considered center-of-mass position evolves slightly different

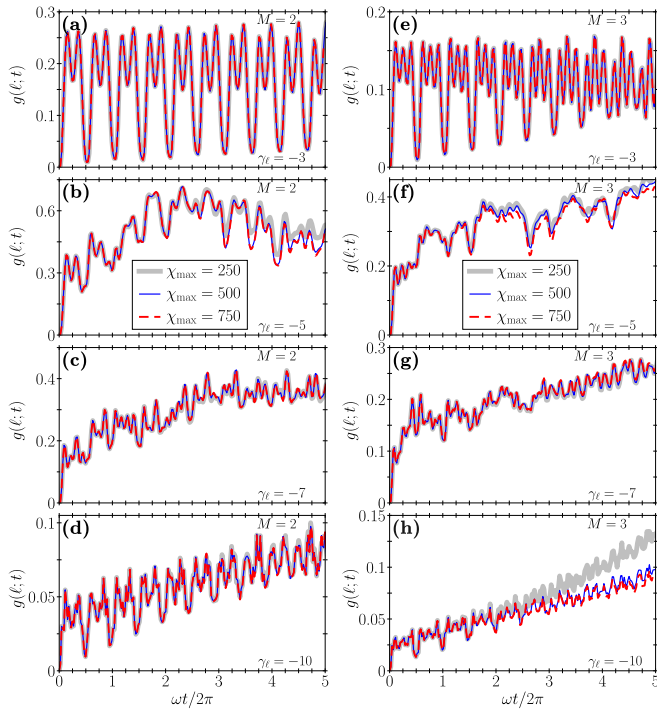


FIG. 11. Comparison between time evolution of  $g(\ell;t)$ , calculated for different beyond-contact attraction strengths  $\gamma_\ell = -3, -5, -7, -10$ , when setting different maximal bond dimension  $\chi_{\max} = 250, 500, 750$ . Left column, (a)–(d), corresponds to the results obtained for  $M = 2$ , while right column, (e)–(h), shows  $g(\ell;t)$  computed in the  $M = 3$  case.

in comparison with the analytical results. Nevertheless, the discretized system behavior is still very similar to the continuous one, which allows us to suppose that conclusions we formulated basing on the analysis performed in the discretized model with  $N_s = 50$  are also valid in the continuous systems.

Second, we show the convergence of our main results determined for  $N_s = 50$  by comparing  $g(\ell;t)$  obtained with different maximal bond dimension  $\chi_{\max} = 250, 500, 750$  for  $M = 2$  and  $M = 3$  and different beyond-contact attraction strengths  $\gamma_\ell = -3, -5, -7, -10$  (see Fig. 11). In addition, in

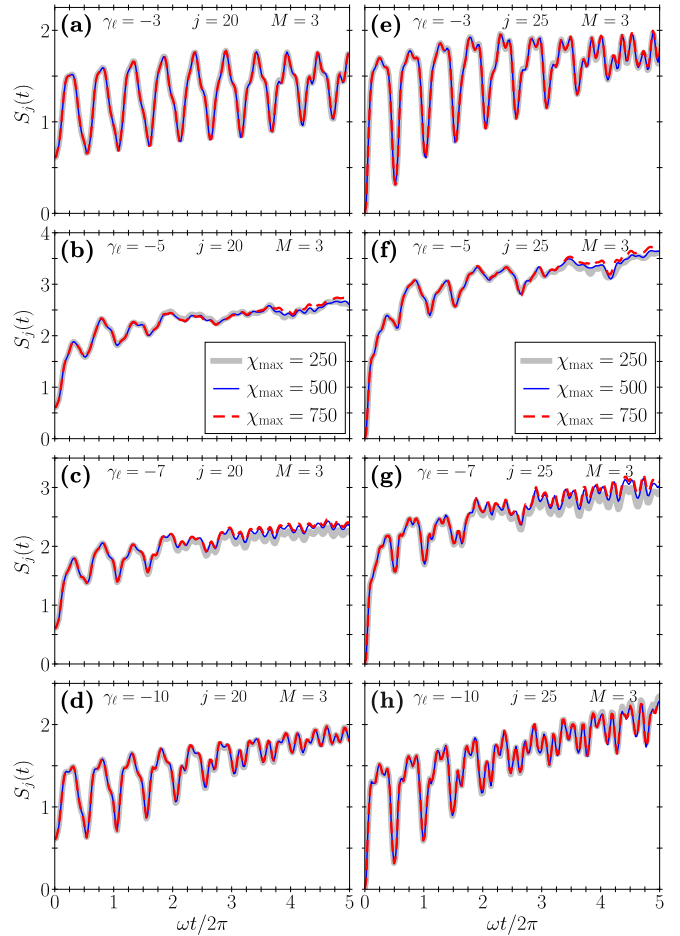


FIG. 12. Time evolution of the von Neumann entanglement entropy  $S_j(t)$  calculated across the bond between  $j$  and  $j + 1$  lattice sites for  $M = 3$ ,  $N_s = 50$ , and two central bonds  $j = 20$  (left column) and  $j = 25$  (right column). The results obtained for different maximal bond dimensions  $\chi_{\max} = 250, 500, 750$  are very similar in the whole considered range of beyond contact attraction strength  $\gamma_\ell = -3, -5, -7, -10$ .

Fig. 12 we present the comparison between dynamics of the von Neumann entanglement entropies,  $S_j$ , calculated across the bond between  $j$  and  $j + 1$  sites for  $M = 3$ , different  $\chi_{\max}$ , and two central bonds  $j = 20, 25$ .

[1] C. J. Pethick and H. Smith, *Bose-Einstein Condensation in Dilute Gases* (Cambridge University Press, Cambridge, UK, 2008).  
 [2] L. Pitaevskii and S. Stringari, *Bose-Einstein Condensation and Superfluidity* (Oxford University Press, Oxford, UK, 2016).  
 [3] S. Giorgini, L. P. Pitaevskii, and S. Stringari, *Rev. Mod. Phys.* **80**, 1215 (2008).  
 [4] M. Brando, D. Belitz, F. M. Grosche, and T. R. Kirkpatrick, *Rev. Mod. Phys.* **88**, 025006 (2016).  
 [5] E. Stoner, *Philos. Mag.* **15**, 1018 (1933).  
 [6] S. S. Saxena, P. Agarwal, K. Ahilan, F. M. Grosche, R. K. Haselwimmer, M. J. Steiner, E. Pugh, I. R. Walker, S. R. Julian, P. Monthoux, G. G. Lonzarich, A. Huxley, I. Sheikin,

D. Braithwaite, and J. Flouquet, *Nature (London)* **406**, 587 (2000).  
 [7] C. Pfleiderer, S. R. Julian, and G. G. Lonzarich, *Nature (London)* **414**, 427 (2001).  
 [8] T. Sogo and H. Yabu, *Phys. Rev. A* **66**, 043611 (2002).  
 [9] T. Karpiuk, M. Brewczyk, and K. Rzażewski, *Phys. Rev. A* **69**, 043603 (2004).  
 [10] R. A. Duine and A. H. MacDonald, *Phys. Rev. Lett.* **95**, 230403 (2005).  
 [11] L. J. LeBlanc, J. H. Thywissen, A. A. Burkov, and A. Paramekanti, *Phys. Rev. A* **80**, 013607 (2009).  
 [12] G. J. Conduit, A. G. Green, and B. D. Simons, *Phys. Rev. Lett.* **103**, 207201 (2009).

- [13] X. Cui and H. Zhai, *Phys. Rev. A* **81**, 041602(R) (2010).
- [14] S. Pilati, G. Bertaina, S. Giorgini, and M. Troyer, *Phys. Rev. Lett.* **105**, 030405 (2010).
- [15] S.-Y. Chang, M. Randeria, and N. Trivedi, *Proc. Natl. Acad. Sci. USA* **108**, 51 (2011).
- [16] D. Pekker, M. Babadi, R. Sensarma, N. Zinner, L. Pollet, M. W. Zwierlein, and E. Demler, *Phys. Rev. Lett.* **106**, 050402 (2011).
- [17] P. Massignan and G. M. Bruun, *Eur. Phys. J. D* **65**, 83 (2011).
- [18] P. Massignan, M. Zaccanti, and G. M. Bruun, *Rep. Prog. Phys.* **77**, 034401 (2014).
- [19] J. Levinsen and M. M. Parish, in *Annual Review of Cold Atoms and Molecules* (World Scientific, Singapore, 2015), pp. 1–75.
- [20] M.-I. Trappe, P. T. Grochowski, M. Brewczyk, and K. Rzażewski, *Phys. Rev. A* **93**, 023612 (2016).
- [21] T. Miyakawa, S. Nakamura, and H. Yabu, *J. Phys. Soc. Jpn.* **86**, 035004 (2017).
- [22] G. M. Koutentakis, S. I. Mistakidis, and P. Schmelcher, *New J. Phys.* **21**, 053005 (2019).
- [23] P. T. Grochowski, T. Karpiuk, M. Brewczyk, and K. Rzażewski, *Phys. Rev. Lett.* **119**, 215303 (2017).
- [24] J. Ryszkiewicz, M. Brewczyk, and T. Karpiuk, *Phys. Rev. A* **101**, 013618 (2020).
- [25] T. Karpiuk, P. T. Grochowski, M. Brewczyk, and K. Rzażewski, *SciPost Phys.* **8**, 66 (2020).
- [26] G. M. Koutentakis, S. I. Mistakidis, and P. Schmelcher, *New J. Phys.* **22**, 063058 (2020).
- [27] B. DeMarco and D. S. Jin, *Phys. Rev. Lett.* **88**, 040405 (2002).
- [28] X. Du, L. Luo, B. Clancy, and J. E. Thomas, *Phys. Rev. Lett.* **101**, 150401 (2008).
- [29] G.-B. Jo, Y.-R. Lee, J.-H. Choi, C. A. Christensen, T. H. Kim, J. H. Thywissen, D. E. Pritchard, and W. Ketterle, *Science* **325**, 1521 (2009).
- [30] A. Sommer, M. Ku, G. Roati, and M. W. Zwierlein, *Nature (London)* **472**, 201 (2011).
- [31] C. Sanner, E. J. Su, W. Huang, A. Keshet, J. Gillen, and W. Ketterle, *Phys. Rev. Lett.* **108**, 240404 (2012).
- [32] Y.-R. Lee, M.-S. Heo, J.-H. Choi, T. T. Wang, C. A. Christensen, T. M. Rvachov, and W. Ketterle, *Phys. Rev. A* **85**, 063615 (2012).
- [33] G. Valtolina, F. Scazza, A. Amico, A. Burchianti, A. Recati, T. Enss, M. Inguscio, M. Zaccanti, and G. Roati, *Nat. Phys.* **13**, 704 (2017).
- [34] A. Amico, F. Scazza, G. Valtolina, P. E. S. Tavares, W. Ketterle, M. Inguscio, G. Roati, and M. Zaccanti, *Phys. Rev. Lett.* **121**, 253602 (2018).
- [35] C. Chin, R. Grimm, P. Julienne, and E. Tiesinga, *Rev. Mod. Phys.* **82**, 1225 (2010).
- [36] F. Scazza, G. Valtolina, A. Amico, P. E. S. Tavares, M. Inguscio, W. Ketterle, G. Roati, and M. Zaccanti, *Phys. Rev. A* **101**, 013603 (2020).
- [37] H. Heiselberg, *Phys. Rev. A* **83**, 053635 (2011).
- [38] A. Recati and S. Stringari, *Phys. Rev. Lett.* **106**, 080402 (2011).
- [39] O. Goulko, F. Chevy, and C. Lobo, *Phys. Rev. A* **84**, 051605(R) (2011).
- [40] F. Palestini, P. Pieri, and G. C. Strinati, *Phys. Rev. Lett.* **108**, 080401 (2012).
- [41] L. He and X.-G. Huang, *Phys. Rev. A* **85**, 043624 (2012).
- [42] L. He, X.-J. Liu, X.-G. Huang, and H. Hu, *Phys. Rev. A* **93**, 063629 (2016).
- [43] P. O. Bugnion and G. J. Conduit, *Phys. Rev. A* **87**, 060502(R) (2013).
- [44] T. Sowiński, T. Grass, O. Dutta, and M. Lewenstein, *Phys. Rev. A* **88**, 033607 (2013).
- [45] S. E. Gharashi and D. Blume, *Phys. Rev. Lett.* **111**, 045302 (2013).
- [46] E. J. Lindgren, J. Rotureau, C. Forssén, A. G. Volosniev, and N. T. Zinner, *New J. Phys.* **16**, 063003 (2014).
- [47] F. Gesztesy and W. Kirsch, *J. Reine Angew. Math.* **1985**, 28 (1985).
- [48] P. Šeba, *Rep. Math. Phys.* **24**, 111 (1986).
- [49] P. Šeba, *Czechoslov. J. Phys.* **36**, 667 (1986).
- [50] T. Cheon and T. Shigehara, *Phys. Lett. A* **243**, 111 (1998).
- [51] T. Cheon and T. Shigehara, *Phys. Rev. Lett.* **82**, 2536 (1999).
- [52] H. Veksler, S. Fishman, and W. Ketterle, *Phys. Rev. A* **90**, 023620 (2014).
- [53] H. Veksler and S. Fishman, *J. Phys. A Math. Theor.* **49**, 085205 (2016).
- [54] K. Jachymski, F. Meinert, H. Veksler, P. S. Julienne, and S. Fishman, *Phys. Rev. A* **95**, 052703 (2017).
- [55] S. Peotta, D. Rossini, P. Silvi, G. Vignale, R. Fazio, and M. Polini, *Phys. Rev. Lett.* **108**, 245302 (2012).
- [56] J. Ozaki, M. Tezuka, and N. Kawakami, *Phys. Rev. A* **86**, 033621 (2012).
- [57] V. R. Pandharipande and H. A. Bethe, *Phys. Rev. C* **7**, 1312 (1973).
- [58] V. R. Pandharipande and K. E. Schmidt, *Phys. Rev. A* **15**, 2486 (1977).
- [59] S. Cowell, H. Heiselberg, I. E. Mazets, J. Morales, V. R. Pandharipande, and C. J. Pethick, *Phys. Rev. Lett.* **88**, 210403 (2002).
- [60] E. Taylor, S. Zhang, W. Schneider, and M. Randeria, *Phys. Rev. A* **84**, 063622 (2011).
- [61] Z.-Q. Yu, S. Zhang, and H. Zhai, *Phys. Rev. A* **83**, 041603(R) (2011).
- [62] P. T. Grochowski, T. Karpiuk, M. Brewczyk, and K. Rzażewski, *Phys. Rev. Lett.* **125**, 103401 (2020).
- [63] R. Jastrow, *Phys. Rev.* **98**, 1479 (1955).
- [64] V. Pandharipande, *Nucl. Phys. A* **178**, 123 (1971).
- [65] S. Moszkowski and B. Scott, *Ann. Phys.* **11**, 65 (1960).
- [66] B. D. Day, *Rev. Mod. Phys.* **39**, 719 (1967).
- [67] G. Pecci, P. Vignolo, and A. Minguzzi, [arXiv:2107.12075](https://arxiv.org/abs/2107.12075).
- [68] M. Łebek, A. Syrwid, P. T. Grochowski, and K. Rzażewski, [arXiv:2107.05594](https://arxiv.org/abs/2107.05594).
- [69] G. E. Astrakharchik, J. Boronat, J. Casulleras, and S. Giorgini, *Phys. Rev. Lett.* **95**, 190407 (2005).
- [70] A. Syrwid, *J. Phys. B: At. Mol. Opt. Phys.* **54**, 103001 (2021).
- [71] T. Busch, B.-G. Englert, K. Rzażewski, and M. Wilkens, *Found. Phys.* **28**, 549 (1998).
- [72] U. Schollwöck, *Ann. Phys.* **326**, 96 (2011).
- [73] R. Orús, *Ann. Phys.* **349**, 117 (2014).
- [74] S. R. White, *Phys. Rev. Lett.* **69**, 2863 (1992).
- [75] S. R. White, *Phys. Rev. B* **48**, 10345 (1993).
- [76] U. Schollwöck, *Rev. Mod. Phys.* **77**, 259 (2005).
- [77] P. Kramer, *J. Phys.: Conf. Ser.* **99**, 012009 (2008).
- [78] M. Yang and S. R. White, *Phys. Rev. B* **102**, 094315 (2020).
- [79] J. Haegeman, J. I. Cirac, T. J. Osborne, I. Pižorn, H. Verschelde, and F. Verstraete, *Phys. Rev. Lett.* **107**, 070601 (2011).
- [80] T. Koffel, M. Lewenstein, and L. Tagliacozzo, *Phys. Rev. Lett.* **109**, 267203 (2012).

- [81] J. Haegeman, C. Lubich, I. Oseledets, B. Vandereycken, and F. Verstraete, *Phys. Rev. B* **94**, 165116 (2016).
- [82] S. Paeckel, T. Köhler, A. Swoboda, S. R. Manmana, U. Schollwöck, and C. Hubig, *Ann. Phys.* **411**, 167998 (2019).
- [83] S. Goto and I. Danshita, *Phys. Rev. B* **99**, 054307 (2019).
- [84] T. Chanda, J. Zakrzewski, M. Lewenstein, and L. Tagliacozzo, *Phys. Rev. Lett.* **124**, 180602 (2020).
- [85] P. Kościk and T. Sowiński, *Sci. Rep.* **8**, 48 (2018).
- [86] J. Viana-Gomes and N. M. R. Peres, *Eur. J. Phys.* **32**, 1377 (2011).
- [87] G. F. Gribakin and V. V. Flambaum, *Phys. Rev. A* **48**, 546 (1993).
- [88] M. Olshanii, *Phys. Rev. Lett.* **81**, 938 (1998).
- [89] T. Bergeman, M. G. Moore, and M. Olshanii, *Phys. Rev. Lett.* **91**, 163201 (2003).
- [90] E. L. Bolda, E. Tiesinga, and P. S. Julienne, *Phys. Rev. A* **68**, 032702 (2003).
- [91] Z. Idziaszek, K. Jachymski, and P. S. Julienne, *New J. Phys.* **17**, 035007 (2015).
- [92] B. Gao, *Phys. Rev. A* **58**, 1728 (1998).
- [93] F. Werner and Y. Castin, *Phys. Rev. A* **86**, 013626 (2012).
- [94] C. L. Blackley, P. S. Julienne, and J. M. Hutson, *Phys. Rev. A* **89**, 042701 (2014).